SCIENCE CHINA
Chemistry

•REVIEWS•

April 2019 Vol.62 No.4: 417–429
https://doi.org/10.1007/s11426-018-9441-4

Metal-organic framework based nanomaterials for electrocatalytic oxygen redox reaction

Kexin Zhang, Wenhan Guo, Zibin Liang & Ruqiang Zou*

Beijing Key Laboratory for Theory and Technology of Advanced Battery Materials, Department of Materials Science and Engineering, College of Engineering, Peking University, Beijing 100871, China

Received December 31, 2018; accepted February 12, 2019; published online March 4, 2019

Due to the severe environmental issues, many advanced technologies, typically fuel cells and metal-air batteries have aroused widespread concerns and been intensively studied in recent years. However, oxygen redox reactions including oxygen evolution reaction (OER) and oxygen reduction reaction (ORR) as the core reactions suffer from sluggish kinetics of the multiple electron transfer process. Currently, Pt, RuO_2, and IrO_2 are considered to be the benchmark catalysts for ORR and OER, but their high price, scarcity and instability hinder them from large-scale application. To overcome these limits, exploring alternative electrocatalysts with low cost, high activity, long-term stability, and earth-abundance is of extreme urgency. Metal-organic frameworks (MOFs) are a family of inorganic-organic hybrid materials with high surface areas and tunable structures, making them proper as catalyst candidates. Herein, the recent progress of MOFs and MOF-derived materials for ORR and OER is systematically reviewed, and the relationship between compositions and electrochemical performance is discussed. It is expected that this review can be helpful for the future development of related MOF-based materials with excellent electrochemical performance.

metal-organic frameworks, oxygen evolution reaction, oxygen reduction reaction, earth-abundant materials, electrocatalysis, nanomaterials

Citation: Zhang K, Guo W, Liang Z, Zou R. Metal-organic framework based nanomaterials for electrocatalytic oxygen redox reaction. *Sci China Chem*, 2019, 62: 417–429, https://doi.org/10.1007/s11426-018-9441-4

1 Introduction

Human society and science technology have made great advances since the first and second industrial revolutions. New technologies and inventions have brought modern society enormous convenience. Nevertheless, almost all these advanced technologies rely on the consumption of unsustainable fossil fuels such as coal and petroleum, which leads to enormous CO_2 emission and severe environmental issues [1]. In order to cope with the climate changes and the depletion of fuel supplies, development of clean energy is of vital importance and urgency. Many advanced technologies like fuel cells, metal-air batteries, and water electrolysis have aroused widespread concerns [2]. The core of these energy conversion technologies is a series of electrochemical reactions, including hydrogen evolution reaction (HER), oxygen evolution reaction (OER), oxygen reduction reaction (ORR) and hydrogen oxidation reaction (HOR) [1]. Compared to HER and HOR, OER and ORR are found to suffer from sluggish kinetics of the multiple electron transfer process [3]. The development of low temperature polymer electrolyte membrane fuel cells (PEMFCs) is severely hampered by the poor performance of the ORR electrodes [4]. OER electrocatalysts also have a serious impact on the development of these energy conversion systems due to the poor durability and the requirement of high overpotentials [5]. Therefore,

*Corresponding author (email: rzou@pku.edu.cn)

the development of highly active electrocatalysts for these two reactions is extremely crucial.

Currently, noble-metal-based composites, such as Pt, RuO_2, and IrO_2 are considered to be the benchmark catalysts for ORR and OER due to their outstanding performance [6]. However, their high price, instability and scarcity hinder them from large-scale application and production. Hence, exploring alternative electrocatalysts with low cost, high activity, long stability, and earth abundance is of extreme urgency [7].

Metal-organic frameworks (MOFs), consisting of coordinated organic ligands and metal ion/cluster centers, are highly porous materials with high surface areas and large pore volumes [8]. In recent years, MOF-based materials including pristine MOFs and MOF composites have been widely used as functional materials in various electrochemical applications [9,10]. Furthermore, MOFs can serve as sacrificial precursors to prepare efficient electrocatalysts [11,12]. The porosity of MOFs can be partially retained after thermal treatment, obtaining high surface-area carbon supports with highly dispersed and exposed active sites [13]. Besides, the heteroatoms (like N, S) in the organic ligands can be incorporated and distributed throughout the whole carbon matrix. Notably, these atoms inserted into the carbon matrix can induce strong charge transfer effects with adjacent C atoms, which has been proven beneficial to ORR and OER process [14]. Unsurprisingly, by virtue of the advantages discussed above, MOF-based materials have been in-depth studied and reported with high performance, implying their enormous potential as the next generation ORR and OER catalysts. By tuning the chemical compositions and morphology of MOF precursors, pyrolysis condition, and construction of various nanostructured composites, the activity of resultant catalysts can be greatly enhanced [15].

In this review, we aim to summarize the strategies for regulating and enhancing the activities of MOF-based ORR/OER electrocatalysts (Figure 1). On this basis, we would like to build connections between rational design and synthesis of MOF-based materials and their catalytic performance. Finally, we will provide some suggestions which might be helpful in the design of MOF-based ORR/OER catalysts, and present an outlook for the future development of MOF-based electrocatalysts.

2 Mechanism for ORR and OER

ORR and OER are two reactions happening in the electrochemically rechargeable metal air batteries. Oxygen molecules are reduced during discharging, while the oxidation process happens during the charging process. However, these two reactions require very different conditions, especially the potential requirements during the reaction process [16].

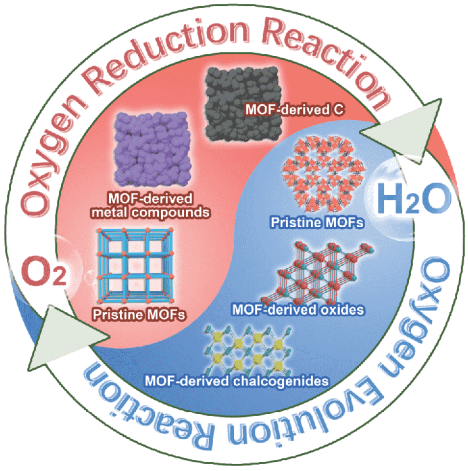

Figure 1 Schematic illustration of MOFs and MOF-derived nanostructures for ORR and OER (color online).

2.1 Mechanism for ORR

The pathway of ORR reaction involves either four-electron or two-electron transfer [17]. A four-electron pathway is more preferred in order to get higher efficiency in the operation of fuel cells, whereas the two-electron pathway is more commonly used in the industrial H_2O_2 production [18]. Generally, three major pathways are proposed for ORR, i.e., the dissociative pathway, the associative pathway, and the peroxo (or 2nd associative) pathway. In either pathway, the initial step is always the diffusion and subsequent adsorption of O_2 on catalyst surface to form an adsorbed O_2 (O_2*, where * denotes a surface site). Dissociative pathway is relatively simple, where the O–O bond breaks upon adsorption prior to any electron and proton transfer, leading to formation of two O* adatom intermediates, followed by successive reduction of the O* into OH* and OH^-. In the associative pathway, addition of the first electron-proton pair to form OOH* takes place before O–O cleavage. The as-formed O* and OH* intermediates are further hydrogenated until OH^- formation. The peroxo pathway can be regarded as a branch of the associative pathway, where the OOH* is firstly reduced to H_2O_2* (an adsorbed hydrogen peroxide). The as-formed H_2O_2* can be further reduced to complete a four-electron pathway, or desorbed from catalyst surface to give free H_2O_2 as the final product, leading to a two-electron reaction [19,20].

Dissociative mechanism:

$O_2+2*\rightarrow 2O*$

$2O*+2H_2O+2e^-\rightarrow 2OH*+2OH^-$

$2OH*+2e^-\rightarrow 2OH^-+2*$

Associative mechanism:

$O_2+*\rightarrow O_2*$

$O_2*+H_2O+e^-\rightarrow OOH*+OH^-$

$OOH*+e^-\rightarrow O*+OH^-$

$O^*+e^-+H_2O \rightarrow OH^*+OH^-$

$OH^*+e^- \rightarrow OH^-+^*$

Peroxo mechanism:

$O_2+^* \rightarrow O_2^*$

$O_2^*+H_2O+e^- \rightarrow OOH^*+OH^-$

$OOH^*+H_2O+e^- \rightarrow H_2O_2^*+OH^-$

(Two-electron pathway: $H_2O_2^* \rightarrow H_2O_2+^*$)

$H_2O_2^* \rightarrow 2OH^*$

$2OH^*+2e^- \rightarrow 2OH^-+2^*$

Choice of the reaction pathways is determined by O_2 dissociating energy barrier on a specific catalyst surface [21]. Typically, the dissociating energy barrier on carbon is usually very high, resulting in two-electron pathway on carbonaceous materials, while on most metal surfaces, ORR will take the four-electron pathway because of the strong adsorption of O_2. As for metal oxides, various pathways exist due to their different compositions or crystal structures [22].

As mentioned above, the binding energies of the intermediates on a specific surface influence the performance of the catalyst. The pioneering work on the ORR volcano plot reports that the oxygen adsorption strength (ΔE_{O^*}) can work as the catalyst activity descriptor [23]. As shown in Figure 2 (a), Pt situates near the top. To achieve the optimal catalytic performance, binding energies on the catalyst surface should be moderate. If the intermediates bind too strongly, the active sites will be occupied, which means the catalyst is poisoned; otherwise if they bind too weakly, the activity is limited due to the difficult activation [16].

2.2 Mechanism for OER

OER is the reverse process of ORR, where H_2O is oxidized to O_2. The overall reaction pathways for OER include several steps, as shown below [25]:

$OH^-+^* \rightarrow OH^*+e^-$

$OH^*+OH^- \rightarrow O^*+e^-+H_2O$

$O^*+OH^- \rightarrow OOH^*+e^-$

$OOH^*+OH^- \rightarrow O_2^*+e^-+H_2O$

$O_2^* \rightarrow ^*+O_2$

In order to drive the OER process, high positive potentials are required, which will lead to the oxidation of metal catalysts. Thus, the kinds of catalysts needed are different from those used in ORR. Most commonly used catalysts are metal oxides. The enthalpy of metal in metal oxides transiting from low to high oxidation state can serve as an activity descriptor [26]. Metal oxides which are difficult to oxidize are not suitable because intermediates are weakly adsorbed; however, metal oxides which are easy to oxidize are also not very active due to the strong adsorption of the intermediates [1]. Recently, an activity descriptor of $\Delta G_{O^*}-\Delta G_{OH^*}$ is proposed which can be applied to a wide variety of metal oxides (Figure 2(b)) [24]. Later, a simple activity descriptor for

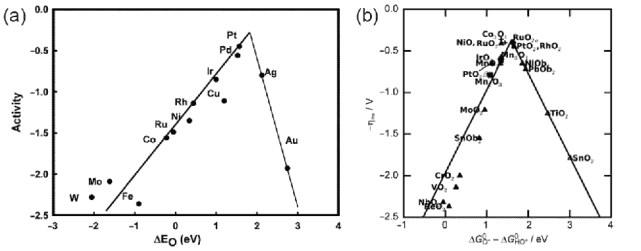

Figure 2 Volcano plots for different electrochemical process. (a) ORR activity plotted as a function of the oxygen binding energy. Reprinted with permission from Ref. [23]. Copyright 2004 American Chemical Society. (b) Activity trends for OER as a function of $\Delta G_{O^*}-\Delta G_{OH^*}$ for Co_3O_4, Mn_xO_y, rutile, and anatase. Reprinted with permission from Ref. [24]. Copyright 2011 John Wiley and Sons.

perovskite oxides, e_g electron occupancy is used to describe the intrinsic OER activities [27]. It shows that the activities depend on the occupancy of 3d electron with an e_g symmetry of surface transition metal cations. The peak OER activity is predicted to be at an e_g occupancy close to unity, and higher covalency of transition metal-oxygen bonds is preferred for OER process.

3 MOFs for ORR

3.1 Pristine MOFs for ORR

Pristine MOFs can be directly used as ORR electrocatalysts, since their abundant pores can facilitate O_2 and water transportation, and rich active metal sites are engaged in this redox-involved electrochemical process [28]. However, few MOFs has been reported with ORR activity, although there are thousands of MOFs discovered. The reasons may be attributed to the instability of MOF structures in aqueous medium and the inferior electrical conductivity which leads to the poor contact between MOF particles and electrode surface [29].

In order to overcome these deficiencies, several strategies have been developed to design MOF structures with high catalytic performance and enhance their electrical conductivity.

Some functional groups in MOFs tend to form interactions with gas molecules, especially the oxygen storage behavior in pores will benefit the ORR process. Transition metal porphyrin complexes, in particular the Fe(III) porphyrins structurally related to hemoproteins, exhibit strong interaction with O_2. Hence, several MOFs containing Fe(III) porphyrins have been reported. A Zr-based porphyrinic MOF, PCN-223-Fe, containing large triangular channels lined up with Fe(III) porphyrin moieties, exhibits high performance in acidic environment. The strong interactions between porphyrin linkers and Zr_6-*oxo*-clusters and the redox inertness of Zr^{4+} ions both contributed to the structure stability during the redox cycling [30].

Cu-BTC as a classic MOF has been widely studied and used in various areas. However, its electrocatalytic performance towards ORR is unstable, mainly due to the structural instability in aqueous media [29]. By introducing 2,2′-bipyridine as an auxiliary ligand to anchor skeleton structure, the more stable Cu-bipy-BTC could be formed. After exposure to water for 24 h, no morphology change was observed, verifying its good stability in aqueous media. Further tests showed the occurrence of ORR activity under the electrocatalysis of Cu-bipy-BTC [31].

Another copper-based MOF (NPC-4) with nanocage structure contains copper active sites (Figure 3(A)) [32]. The windows of the nanocages with diameters of ~0.6 nm were large enough for gas molecules to pass through, however the pores were occupied by solvent DMA molecules in the as-synthesized MOF. Without activation, the electrochemical performance mainly depended on the electron transport between electrode and some metal ions near the electrode surface. After activation by a solvent-exchange method, space inside the nanocages could be liberated, exposing plenty of open metal sites (Figure 3(B)). By removing the solvent molecules occupied in the nanocage, dissolved oxygen could enter into the nanocages and be reduced by Cu^{+} (Figure 3(C)).

The instability of MOF structures in aqueous medium and the inferior electrical conductivity result in the poor performance of pristine MOFs, and therefore few MOFs has been reported with ORR activity. Thus, construction of aqueous stable MOFs and introduction of functional groups in MOFs to enhance the conductivity could guide the synthesis of highly efficient MOF catalyst. Besides pristine MOFs, many efforts have been made to develop efficient MOF composites to increase the electrical conductivity. In particular, by assembling functionalized graphene with MOFs [32–34], or embedding highly active metal compounds into MOF matrices [28,35], their ORR performances and stabilities could be significantly improved.

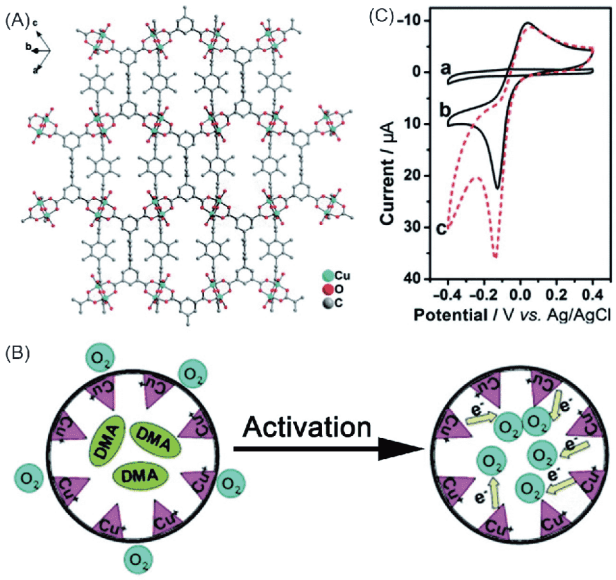

Figure 3 (A) Crystal structure of NPC-4. (B) Schematics for O_2 reduction catalyzed by as-prepared NPC-4 and activated NPC-4. (C) CV curve a, b, c of RGO, activated NPC-4 modified RGO/GCE in N_2-saturated PBS solution, activated NPC-4 modified RGO/GCE in O_2-saturated PBS solution, respectively. Reprinted with permission from Ref. [32]. Copyright 2014 Royal Society of Chemistry (color online).

3.2 MOF derived materials for ORR

With tunable and various structures, MOFs can serve as precursors to prepare highly porous carbon-based materials or metal-carbon composites by pyrolysis. To some extent, their structural ordering and porosity can be preserved. In addition, the stability of MOF-derived materials is enhanced, which endows them with superior durability under continuous operation and harsh reaction conditions.

3.2.1 Creation of metal-free ORR active sites

MOFs have been widely used to produce various porous carbon materials. Since some metals with low boiling point can evaporate during pyrolysis or can be leached by acid after pyrolysis, the metal-free carbon composites can be easily obtained. Besides, heteroatom-doping can generate uneven charge distribution throughout the carbon network, leading to favorable chemisorption of O_2.

ZIF-8 is the most popular MOF as precursor for pyrolysis because the evaporative Zn in the framework can act as a pore-forming agent during calcination, creating plenty of open channels. Unlike the amino ligands in many other MOFs, the 2-methylimidazole (2-MeIM) ligands in ZIF-8 are rich in N and free of O. Thus, using ZIF-8 as precursor can create a uniform distribution of N in the carbon frameworks. In addition, the carbon precursor 2-MeIM can produce a much higher degree of graphitization in the obtained carbon frameworks compared to non-aromatic carbon precursors [36]. As early as 2014, Zhang *et al*. [37] had studied the influence of pyrolysis temperature and carbonization time on the ORR performance of ZIF-8. Generally, higher activity was expected for pyrolysis at higher temperature. However, longer carbonization time did not proportionally contribute to higher electrochemical activity. Only the synergistic contributions of high surface area, high degree of graphitization and high graphitic N atom content could result in the optimum electrocatalytic activity. Nevertheless, the best performance they got showed an ORR onset potential 40 mV lower than that of Pt/C, indicating that direct MOF pyrolysis without additional modification was difficult to prepare efficient ORR catalysts. By *in situ* growing ZIF-8 on graphene oxide (GO), followed by thermal treatment, the resultant catalyst exhibited a high activity, good tolerance to methanol and superior stability compared to Pt/C [38].

Introduction of heteroatoms which are rare in MOF ligands

is another way to enhance the performance. After carbonization at high temperature, and followed by thermal treatment with NH_3 and thiourea, ZIF-8 converted into N,S-coupled doped carbon networks. First principles calculations (as shown in Figure 4) revealed that the coupled dopants had higher activity compared to isolated dopants, providing a great electron density to the adsorbed O_2, thus originating enhanced ORR activity [39]. Also, after modified with boron-containing reactants and treated at high temperature, ZIF-8 derived hollow N/B co-doped carbon exhibited a pronounced ORR activity with an onset potential of −0.12 V (vs. Ag/AgCl) along with superb long-term stability [40].

Moreover, there are some other methods to modify the pore size and enhance the electrical conductivity of ZIF-derived composites, such as NaCl-assisted exfoliation approach [41–43], NH_3 activation approach [44], self-sacrificial template approach [45], and incorporation with additional carbon sources [46]. Besides ZIF-8, other kinds of Zn-MOFs (for example Zn-MOF-74 [47,48], ZIF-7 [49], and MOF-5 [50]) can also serve as the precursors to prepare metal-free ORR electrocatalysts.

3.2.2 Creation of non-precious metal ORR active sites

As discussed above, because of the instability of MOF structures in the aqueous medium, few MOFs has been reported with remarkable activity for ORR. Thus, MOFs can serve as precursors to prepare highly porous carbon-based transition metal compounds. To some extent, their structural ordering and porosity can be preserved. In addition, the stability of MOF-derived materials will be greatly enhanced. In the most cases, carbon layers will form, surround and protect the transition metal nanoparticles, which can endow them with superior durability under continuous operation and harsh reaction conditions. Significant efforts have been made to illustrate the active sites in M–N–C catalysts. Two types of active sites including metal-nitrogen moieties embedded in carbon (MN_xC_y) and nitrogen doped carbon encapsulating inorganic metal species ($M@N_xC_y$) have been proven to show ORR activity. The phenomenon of agglomeration of metal nanoparticles would happen when pyrolyzing the sole MOF-precursor, leading to the large grain size and inhomogenous distribution. Since some metals such as Zn with low boiling point can evaporate during pyrolysis, introducing Zn metal sites into MOFs to produce bimetallic MOFs can be a method to avoid the agglomeration of metal nanoparticles during pyrolysis. The carbonized MOF-derived composites can also be leached by acid after pyrolysis, thus the large particles will be removed. Furthermore, heteroatom-doping can generate uneven charge distribution throughout the carbon network, and further influence the electronic structure of the transition metal nanoparticles.

By pyrolysis of ZIF-67, N-doped carbon nanopolyhedrons decorated with Co nanoparticles have been fabricated. When

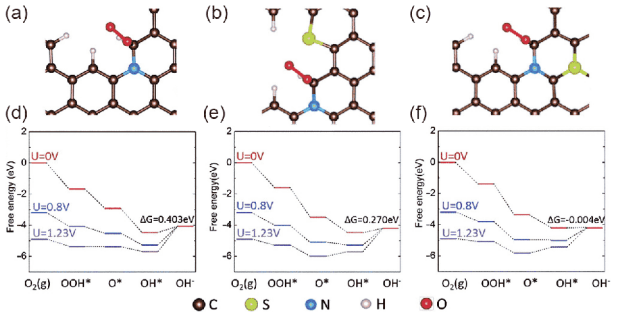

Figure 4 Optimized structures for the stable adsorbed O_2 on (a) N-doped nanocarbon, (b) N,S-isolated nanocarbon, and (c) N,S-coupled nanocarbon. Free-energy diagram of ORR on (d) N-doped nanocarbon, (e) N,S-isolated nanocarbon, and (f) N,S-coupled nanocarbon in alkaline media. Reprinted with permission from Ref. [39]. Copyright 2017 Royal Society of Chemistry (color online).

precisely adjusting the MOF particle size and pyrolysis temperature, the smallest ZIF-67 (300 nm) calcinated at 750 °C exhibited superior ORR performance with an onset potential of 0.86 V and a half-wave potential of 0.71 V in acidic solution [51]. In order to avoid the agglomeration of metal nanoparticles, strategy of incorporation with another metal species with low boiling point (for instance, Zn) into the MOF precursor can be adopted. The composition, morphology and ORR activity of bimetallic CoZn-ZIF-derived Co–N–C could be tuned by different Zn/Co ratio. The presence of Zn formed a spatial isolation of Co which suppressed its sintering. High surface area could also be obtained after Zn evaporation. The optimal Co–N–C exhibited remarkable ORR activity for all pH values, even with a half-wave potential 30 mV more positive than Pt/C in 0.1 M KOH [52]. Also, introducing evaporative sacrificial templates [53–56] and additional N,C sources [57–59] would create hierarchical porous systems with higher surface area, more active site exposure and higher electrical conductivity.

As early as 1964, Co phthalocyanine had been discovered with ORR activity [60]. Since then, the heat-treated M–N–C ORR catalysts have been extensively studied. Such kind of catalysts are generally prepared by pyrolyzing a composite precursor which contains Fe or Co, N, and C at high temperature to obtain robust structure and high activity. The ORR active sites are thought to be N coordinated metal sites. You *et al*. [61] studied the conversion of ZIF-67 to CoNC via pyrolysis in the temperature range of 600 to 1000 °C. The catalyst obtained at 900 °C possessed the morphology of carbonaceous species similar with MOF backbone, and Co particles sized in the range of 8–15 nm were homogenously distributed within the carbon matrix. It showed the best ORR performance among all the obtained catalysts and could be further applied into the microbial fuel cell. The authors verified that the target catalysts consisted of metallic Co and Co–N_x species, which acted as the ORR active catalytic sites. Such structure could offer more active sites. Co@NC na-

nostructures converted from Zn_xCo_{1-x} MOF structures showed excellent catalytic activity for ORR, with an onset potential of 0.97 V, half-wave potential of 0.88 V and superior durability with zero degradation after 5000 cycles. X-ray photoelectron spectroscopy (XPS) analysis showed the presence of CoN_x–C_y and Co–N_x active sites, which were known to be highly active towards ORR [62].

Inspired by the reported results that the binuclear sites in macrocycle compounds exhibit higher catalytic activity than the single-center sites [63], Xiao *et al*. [64] designed a novel binuclear active site structure, Co_2N_5, by precisely controlling the structure of bimetallic MOFs. The binuclear sites were directly observed by aberration corrected scanning transmission electron microscopy (Figure 5(a, b)). The configuration was determined by extended X-ray absorption fine structure (EXAFS) combined with DFT calculation. Amazingly, Co_2N_5 site outperformed the conventional CoN_4 site with 12 times higher activity due to the decreased energy barrier during ORR process (Figure 5(c, d)).

Fe–N_x/C catalysts are regarded more active than Co–N_x/C catalysts. Still, a fact must be declared that although Fe–N_x/C has higher activity, Co–N_x/C is more stable. A way to enhance the performance of Fe–N_x/C catalyst is to increase the density of FeN_x. However, simply raising the Fe concentration during the synthesis is not effective, because it will lead to Fe aggregation and generate inactive Fe compounds at the same time. Wang *et al.* [65] reported a method to dope Fe into ZIF-8 by partially replacing Zn ions. As a result, Fe was uniformly distributed into the framework with well-defined Fe–N_4 coordination. Without the need for additional post-treatment such as acid leaching and second heating treatment, only one-step thermal treatment was needed. Notably, the control of O_2-free environment for stabilizing Fe(II) was crucial for generating uniform Fe distribution without any agglomerated Fe particles. The new catalyst exhibited very high ORR activity in terms of its half-wave potential as high as 0.82 V and extremely low H_2O_2 yield. A consensus has been reached that a different coordination structure of Fe–N_x will lead to variations in electrocatalytic activity for ORR. Lai *et al.* [66] proposed a host-guest chemistry strategy (Figure 6(a)) to construct Fe-mIm nanoclusters@ZIF-8 and further transformed it into Fe–N/C with tunable structures. ZIF-8 host exhibited a significant confinement effect during pyrolysis process, resulting in different types of Fe–N_x sites. From X-ray absorption near edge structure (XANES) and EXAFS spectra, this host-guest chemistry strategy could successfully protect Fe–N_x sites from transformation into inorganic phases after high temperature pyrolysis, and assist in forming five-coordinated Fe–N_x bonds. The electrocatalytic performance proved that the five-coordinated Fe–N_x sites could promote ORR more effectively than low coordination number sites. Figure 6(b, c) show the trends of calculated free energy for every intermediate on different

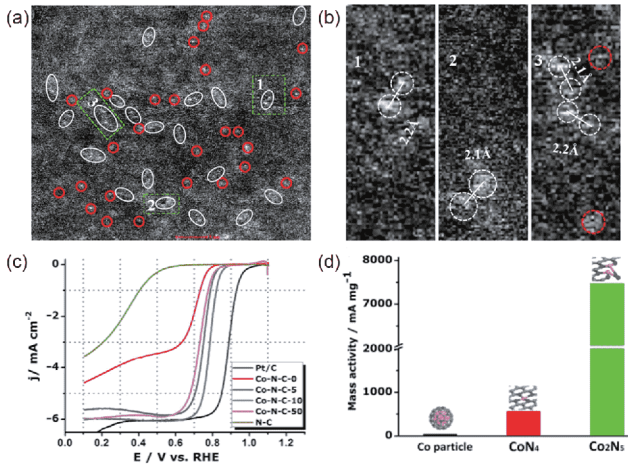

Figure 5 (a) Aberration-corrected HAADF-STEM image of Co–N–C-10. (b) Magnified image marked in (a). (c) ORR polarization curves for Co–N–C-*x*, N–C and commercial Pt/C catalysts in O_2-saturated 0.1 M $HClO_4$. (d) Comparison of mass-specific activity of each active site structure. Reprinted with permission from Ref. [64]. Copyright 2018 Elsevier (color online).

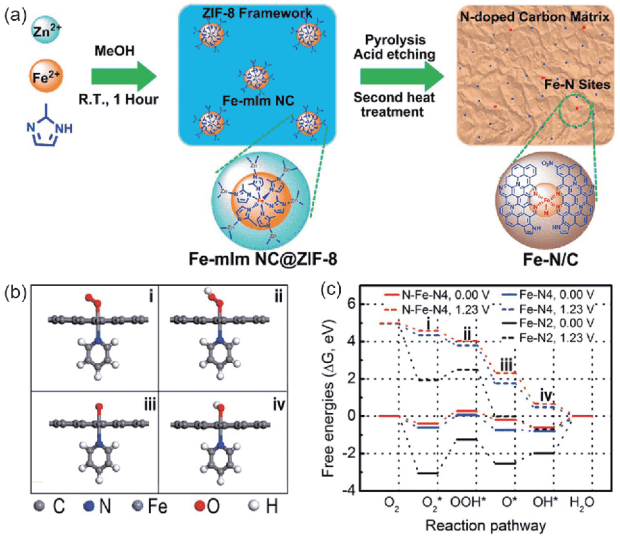

Figure 6 (a) Schematic illustration of the host-guest chemistry strategy. (b) Optimized structures of (i) O_2, (ii) OOH, (iii) O, and (iv) OH adsorbed on N–Fe–N_4. (c) Free-energy diagrams of the reduction of O_2 to H_2O on the N–Fe–N_4, Fe–N_4, and Fe–N_2 structures in acid media. Reprinted with permission from Ref. [66]. Copyright 2017 American Chemical Society (color online).

coordination sites. Compared to Fe–N_2, a decreasing free energy for all intermediates was observed on N–Fe–N_4 and Fe–N_4 at 0 V, suggesting that ORR could happen more easily on these two structures than on Fe–N_2. When a potential of 1.23 V was applied, an adsorption reaction was observed on these three structures with an obvious reaction energy barrier. Anyway, N–Fe–N_4 showed a lower energy barrier (0.67 eV) than Fe–N_4 (0.75 eV) or Fe–N_2 (1.99 eV), which meant O_2 could be completely reduced to H_2O easily [66].

In addition to Fe–N_x, Fe_3C sites also exhibit high ORR activity, which can be prepared from MOFs. Hierarchical

porous N-doped carbon with Fe/Fe_3C nanoparticles were prepared by carbonization of ZIF-8 (as a sacrificing template) and potassium ferricyanide (as an iron precursor). The obtained catalyst had high amount of Fe–N_x sites coexistence with Fe/Fe_3C nanocrystals. The authors demonstrated that the ORR activity of Fe–N_x could be boosted by adjacent Fe/Fe_3C nanocrystals, while the encapsulated Fe/Fe_3C could activate the surrounding graphitic carbon layers to enhance ORR activity [67].

3.2.3 Creation of single-atom active sites

Single-atom catalysts (SACs) with isolated metal atoms dispersed on solid supports have attracted extensive research attention. Conventional heterogeneous catalysts usually contain a broad size distribution of metal particles. However, only a portion of particles with suitable sizes can serve as catalytic species, while other particles may be inert or lead to undesired reactions, resulting in a low metal utilization efficiency and thereafter a high metal consumption and low gravimetric activity. The development of SACs can enable the sufficient use of metal resources and facilitate atomic-utilization efficiency.

Recently, Zhang *et al*. [68] reported an ORR catalyst with atomic level dispersion of Fe sites based on bimetallic strategy. The aberration corrected electron microscopy and EXAFS of K-edge of Fe confirmed that there were highly dispersed FeN_4 sites without aggregated Fe particles inside the porous carbon. This catalyst showed a half-wave potential of 0.85 V, only leaving a 30 mV gap with Pt/C in acidic media. Due to the presence of Fe in electrodes may generate free radicals causing serious degradation of the membrane (that is the Fenton reaction), Fe-free cathode catalysts are therefore demanded in practical industry applications. Similarly using the bimetallic strategy, Co-doped ZIF-8 precursors could convert into a high-performance nitrogen-coordinated single Co atom catalyst, which are verified by high-angle annular dark-field (HAADF) scanning transmission electron microscope (STEM) coupled with electron energy loss spectroscopy (EELS). This atomically dispersed CoN_4 catalyst showed exceptional ORR activity and stability in acidic media with a half-wave potential of 0.80 V, which was comparable to Fe–N–C catalysts [69].

Carbon corrosion of catalysts will lead to the dissolution of metal sites, which induces significant charge and mass transport resistances due to the changes of carbon lattice structures and morphologies. Thus, high degree of graphitization is vital to enhance the resistance of the catalysts. Mn doping has been discovered to promote the stability of nanocarbon catalysts and catalyze graphitic structures. More importantly, Fenton reactions can be restrained because of the weak reactivity between Mn and H_2O_2. However, Mn ions cannot easily exchange with Zn and form complexes with N, and Mn aggregates easily during carbonization even at a low content. Synthesizing carbonaceous catalysts with a high content of atomically dispersed MnN_4 sites is therefore a quite challenging target. Recently, Li *et al.* [70] reported a catalyst with atomically dispersed MnN_4 sites obtained through a two-step doping and adsorption processes from ZIF-8 precursor (Figure 7(a)). The Mn content in the obtained catalyst was comparable to other atomically dispersed Fe and Co ones, avoiding the formation of unstable and inactive metallic compounds during the heat treatment. Evidence for the embedding atomic MnN_4 sites within the carbon matrix was established by X-ray absorption spectroscopy, aberration corrected electron microscopy, and medium-angle annular dark field (MAADF) STEM coupled with EELS (as shown in Figure 7(b, c)). The Mn–N–C catalyst exhibited a half-wave potential of 0.80 V, approaching that of Fe–N–C catalyst, along with significantly enhanced stability in acidic media (Figure 7(d)). First-principles calculations further supported that MnN_4 sites could promote ORR activity via a $4e^-$ pathway in acidic media.

4 MOFs for OER

Researches towards MOF-based OER catalysts are less than those related to ORR since major suitable catalysts are oxides and hydroxides of transition metals. Actually, MOFs are becoming much more popular for OER. The metal-ligand coordination sites are allowed to prepare some novel OER active sites. Combination of MOFs with different substrates enables further enhancement in the catalyst activity. Furthermore, MOFs can act as the sacrificial templates to produce different metal compounds for utilization in the OER process.

4.1 Pristine MOFs for OER

Benefitting from the tunable structures, the catalytic active sites of MOFs can be modified by introducing heteroatoms/ligands or creating unsaturated coordination environment for enhanced performance. Converting traditional bulk MOFs into 2D nanosheets can greatly enhance the electrocatalytic activity due to several advantages [71]. First, high percentage of active sites will expose with increased surface areas. Second, nanoscale thickness ensures rapid mass transport and charge transfer. Two-dimensional ultrathin MOF nanosheets (NiFe-UMNs) were synthesized through a simple ultrasonic oscillation method. 2D layered structure could be clearly certified by using TEM and atomic force microscope (AFM) (Figure 8(a, b)). NiFe-UMNs exhibited superior activity with a low onset potential of 1.45 V and a low overpotential of 260 mV to reach 10 mA cm^{-2} in alkaline electrolyte. High durability of the nanosheets was also confirmed by maintaining at an overpotential of 280 mV for

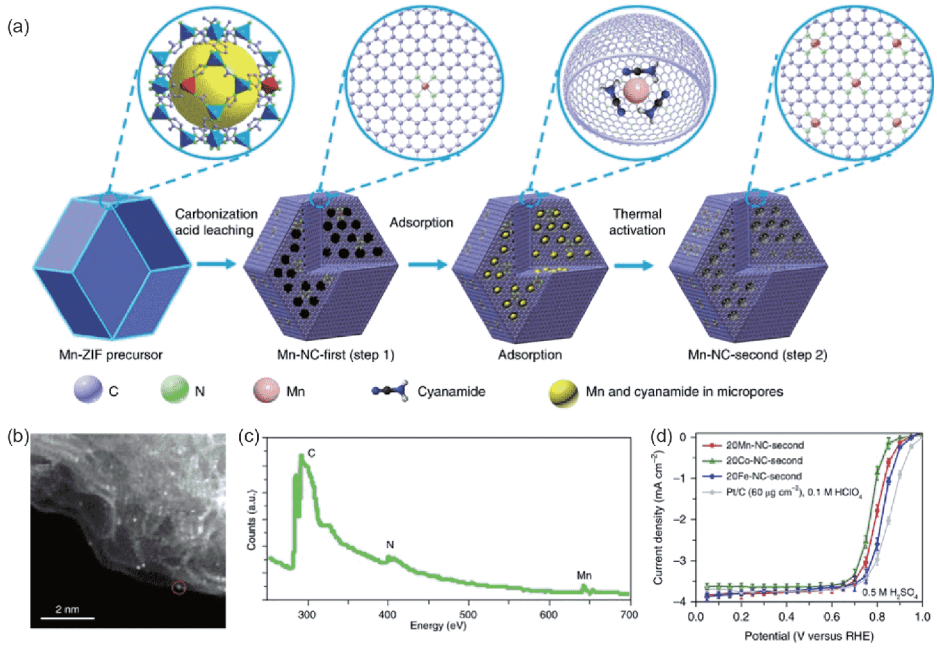

Figure 7 (a) Schematic illustration of atomically dispersed MnN_4 site catalyst synthesis. (b) Aberration-corrected MAADF-STEM image. (c) EEL point spectrum from the atomic site circled in red in (b). (d) Comparison of the catalytic activity of Fe–, Co– and Mn–N–C catalysts prepared from identical procedure. Reprinted with permission from Ref. [70]. Copyright 2018 Springer Nature (color online).

10000 s, and only 4.8% current loss was detected (Figure 8 (c, d)). DFT calculations demonstrated that NiFe-UMNs had a much lower energy barrier for OH^*, and XPS showed that the addition of Fe could generate higher valence state Ni, which possessed a stronger ability of accepting electrons and accelerated the charge transfer. Additionally, the combination of Ni and Fe could optimize the filling of e_g-orbit and further enhance the catalytic activity for OER [72]. Another 2D shaped NiCo-UMOFNs exhibited OER activity with an overpotential of 250 mV to achieve a current density of 10 mA cm^{-2} and current density unchanged between 1.50 and 1.52 V for 10000 s. The coordinatively unsaturated metal sites and coupling effect between Co and Ni contributed to this high performance [73].

By directly growing MOFs on nickle foam (NF), the OER performance would be further enhanced. Recently, Li *et al.* [74] partly replaced the FeO_6 octahedrons with NiO_6 ones in MIL-53 and obtained Fe/Ni bimetallic MOFs. When introducing the third metal ions (Co^{2+}) and growing MOFs on the NF, the OER performance could be further enhanced compared to Fe/Ni-MIL-53, which was among the best OER catalysts reported to date. The optimized Fe/Ni/Co-MIL-53 could reach a current density of 20 mA cm^{-2} at a low overpotential of 236 mV with a small Tafel slope of 52.2 mV dec^{-1}. The incorporation of Fe could lead to higher valence of Ni and Co, which was crucial in modulating electronic properties of Ni, thus all these factors promoted the OER activity. Although great efforts have been made to improve the performance and stability of pristine MOFs, the skeleton of MOFs may generate inevitable changes due to the high positive potentials applied during the OER process, which are not clear yet. *In-situ* characterization techniques and computational methods can give information about the reaction process and provide guidance for catalyst design.

4.2 MOFs derived materials for OER

4.2.1 Conversion of MOFs into metal nanoparticles

3d transition metals (for example, Fe, Co, Ni) and their alloys have high intrinsic activities for OER. However, bulk or aggregated particles have no distinct advantages due to their low specific surface areas and few exposed active sites. Furthermore, the bare 3d transition metals under strong alkaline media and high overpotentials are not stable. Actually, metal nanoparticle-based catalysts are rare because the OER potential is high enough to oxidize most non-noble metals. To improve the performance, encapsulating these nanoparticles into graphene or carbon nanotubes can be an effective method.

By annealing Ni-MOF in N_2 atmosphere, Ni nanoparticles encapsulated in few-layer N-doped graphene (Ni@NC) were obtained. By controlling the annealing temperature, graphene layers surrounding Ni nanoparticles with suitable thickness and conductivity could be generated, where electrons transferred from Ni cores to graphene layers. The N-doping could tune the binding energies of reaction intermediates and the corresponding activity. It was observed that the surface of Ni was partially oxidized, which could also act

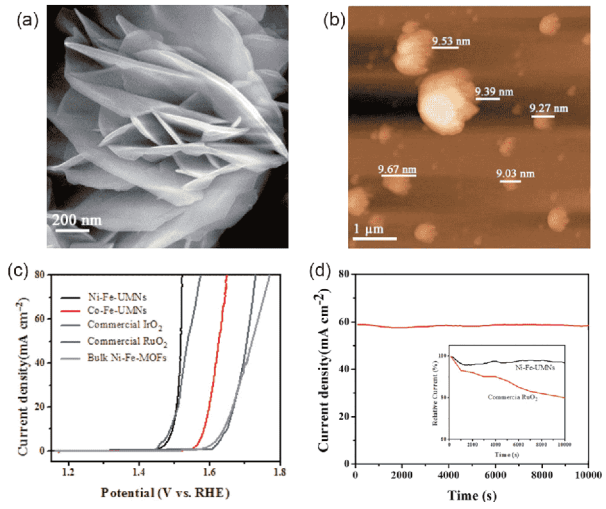

Figure 8 (a) SEM image, (b) AFM image of NiFe-UMNs. (c) LSV curves of NiFe-UMNs, CoFe-UMNs, bulk NiFe-MOFs, commercial RuO_2 and IrO_2 in O_2-saturated 1 M KOH. (d) Chronoamperometric curves for long term stability tests of NiFe-UMNs at the constant overpotential of 0.28 V and the inset is the comparison with commercial RuO_2 (red curve). Reprinted with permission from Ref. [72]. Copyright 2018 Elsevier (color online).

as active sites [75].

The porous Ni NF as a substrate can augment the electrode-electrolyte interface and minimize ohmic loss. Growing stacked lamellar Ni(BDC) sheets on the NF prior to high-temperature annealing constructed a hierarchical architecture. Ni nanoparticles provided active sites, and the carbon matrix offered conductive pathways as well as protection to the Ni nanoparticles. Additionally, after high-temperature calcination, the lamellar structure slightly expanded, which further facilitated the infiltration of electrolytes and enhanced the mass and charge transportation. With this advanced architecture, the catalyst afforded a current density of 10 mA cm^{-2} at a overpotential of 265 mV [76].

When using trimetallic ZIF (FeNiZn-ZIF) as the pyrolysis precursor, catalyst containing FeNi alloy nanoparticles encapsulated in N-doped CNT was obtained. It reached 10 mA cm^{-2} with a 300 mV overpotential and exhibited a low Tafel slope of 47.7 mV dec^{-1}. The TEM image revealed that FeNi alloy nanoparticles were embedded at the terminals of CNTs. XPS spectrum showed that there was no metal oxide/hydroxide formed even after long-term electrolysis process. Thus, the OER active sites were determined to be FeNi alloy instead of FeNi oxide/hydroxide [77].

Co nanoparticles encapsulated in graphitic carbon can also act as OER catalyst [78–80]. Actually, the surface oxidized Co formed during the OER process is thought to be the active site. The synergistic cooperation of *in situ* formed oxidized Co layers and metallic Co cores plays an important role in enhancing the OER performance. The metallic Co underneath is a current reservoir to provide electron pathways to the outer oxidized Co.

4.2.2 *Conversion of MOFs into metal oxides*

As discussed in the section above, during the OER process, metal nanoparticles will transform into oxidized forms, and the actual active sites are often the oxidized metal composites. Therefore, directly converting MOF precursors into metal oxides by high-temperature pyrolysis is a more straightforward way.

A series of layered 2D MOFs were fabricated and acted as templates to construct metal oxide/carbon (MO_x/C, M=Co, Ni, and Cu) nanosheets arrays for OER. The resulting highly oriented arrays displayed improved activity and durability. After pyrolysis, an opened-up network structure constructed by the interconnected 2D nanosheets could be obtained. The 2D arrayed structure incorporated with C could help rapid decomposition of OH^*, which enhanced the OER activity. This method could even grant the poorly active Cu_2O-based catalysts with high performance in terms of both activity and durability [81].

Similar to MOF-derived ORR catalysts, bimetallic oxides derived from MOFs could also promote the OER activity. The replaceable nature of metal cations in MOFs makes it easy to tune the calcined products. In the study by Lu *et al.* [82], porous $CoFe_2O_4$/C composites were obtained by one-step pyrolysis of MOF-74-Co/Fe nanorod arrays. The catalyst exhibited excellent activity and stability (a low potential of 1.47 V at 10 mA cm^{-2} and ~7.5% potential increase at 100 mA cm^{-2} for 60 h). Xu *et al.* [83] synthesized C-confined NiCo@$NiCoO_2$ core@shell nanoparticles by carbonization of the bimetallic NiCo-MOF microrod arrays (Figure 9(a–c)). The oxygen vacancies in these arrays could significantly improve the conductivity of $NiCoO_2$ and accelerate the kinetics of oxidation reactions (Figure 9(d)). Interestingly, there existed the Schottky barriers between NiCo and $NiCoO_2$, which could also obviously enhance the conductivity.

Recently, molybdenum-based compounds have been frequently used as composition tuning agents and are found to promote the electrocatalytic activity and stability. Using MOFs loaded with Mo source as precursors, the derivative hybrid structure will be a good candidate for OER. Well-defined 3D nanowire-assembled hybrid materials of CoO_x-MoC/NC were fabricated. The formation of CoO_x-MoC heterostructures and their synergistic effect facilitated the reaction kinetics, leading to an onset overpotential of merely 290 mV, and a low overpotential of 330 mV to afford a current density of 10 mA cm^{-2} [84]. Another novel nanocage-structured CoO-MoO_2 composite was designed by using ZIF-67 as template. The incorporation of Mo could protect the nanocage structures from collapsing. The formation of conductive MoO_2, the enlarged surface area and the intrinsic activity of CoO all contributed to the high performance of CoO-MoO_2 (η=312 mV at 10 mA cm^{-2} as well as good stability) [85].

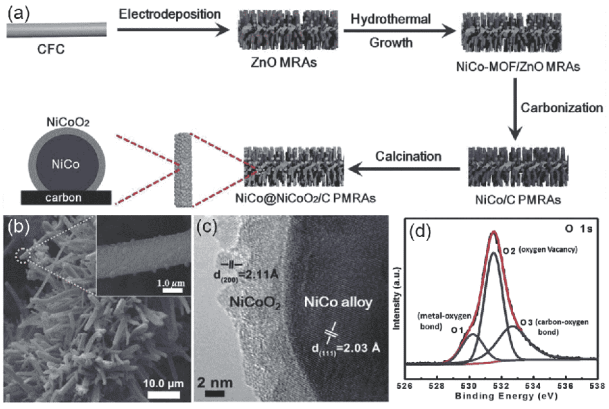

Figure 9 (a) Schematic illustration for the fabrication of Ni-Co@Ni-iCoO2/C PMRAs. (b) SEM image, (c) HRTEM image of a typical Ni-Co@$NiCoO_2$ core-shell nanoparticle. (d) High resolution XPS spectra of O 1s of NiCo@NiCoO2/C PMRA. Reprinted with permission from Ref. [83]. Copyright 2018 John Wiley and Sons (color online).

4.2.3 *Conversion of MOFs into metal chalcogenides*

Transition metal chalcogenides, namely, sulfides and selenides, have become robust earth-abundant OER catalysts with the capacity to lower the overpotential. Especially, cobalt chalcogenides are attracting lots of attention. However, the poor electrical conductivity makes the performance of cobalt chalcogenides unsatisfactory. Thus, growing or supporting them on the conductive carbon-based substrates can be an effective way.

Wu *et al*. [86] prepared Co_9S_8 nanoparticles-embedded N/S-codoped carbon nanofibers through calcinating the core-shell ZIF-wrapped CdS nanowires. During the pyrolysis, CdS was reduced by carbon to produce evaporative Cd metal and release S. As a result, S could react with Co to form Co_9S_8 and insert into the carbon matrix to form N/S-codoped carbon. The annealed product inherited the morphology of the precursor, giving rise to a large surface area and providing abundant accessible active sites. Consequently, a low overpotential of 302 mV at 10 mA cm^{-2} and a small Tafel slope of 54 mV dec^{-1} were achieved. Another Co/Co_9S_8 core-shell structure anchored onto N/S-codoped porous graphene sheets was fabricated by pyrolyzing the S,N-containing dual organic ligands assembled Co-MOFs on graphene oxide. The results showed that the obtained catalyst could afford an overpotential of 290 mV at a current density of 10 mA cm^{-2}, slightly better than that of commercial RuO_2 [87].

Cobalt selenides can also participate in the OER process. Co-MOF-74 derived $CoSe_2$ [88], ZIF-67 derived $Co_{0.85}Se$ [89], and bimetallic NiFe-MOF derived $NiSe_2/Fe_3Se_4$ hybrids [90] all exhibited good performance and high stability. Specially, tellurium possesses the intrinsic metallic feature different from O, S, and Se, and for $CoTe_2$, the 3d electrons of Co adopt a low-spin coordination in the form of $t_{2g}^6e_g^1$, providing $CoTe_2$ metal conductivity. Thus, the metallic properties of $CoTe_2$ made it proper to perform as an OER catalyst [91,92].

4.2.4 *Conversion of MOFs into metal phosphides*

Transition metal phosphides (TMP) are promising participants for OER due to their high abundance, low cost, and great acid-base stability in the pH range of 0–14. Compared to monometallic phosphides, the dopants and the host metal atoms in homo-bimetallic phosphides have charge transfer and their electronic structures can be optimized to reduce the kinetic energy barriers during the catalytic processes.

The Co_4Ni_1P nanotubes were prepared via low temperature phosphorization from CoNi-MOF-74. It has been reported that Ni is more beneficial for desorption of OH^-, while Co has higher activity for the Tafel steps. Hence in Co_4Ni_1P, the surface Ni accelerated water dissociation with high efficiency and Co made gas generation and release easy [93]. In another work by He *et al.* [94], ZIF-67 nanocubes first formed NiCo-LDH on the surface, and then converted into novel NiCoP/C nanoboxes by phosphorization (Figure 10). The obtained NiCoP/C nanoboxes had a much larger electrochemical active surface area (ECSA) and a much lower electron-transfer resistance. During the OER process, the surface Ni and Co cations were partially oxidized into NiOOH and CoOOH. Thus, Ni_2P/NiOOH and CoP/CoOOH core-shell structures were the actual active sites. More interestingly, tricomponent metal phosphides ($CoNi_{0.2}Fe_{0.05}$-Z-H-P) were synthesized and proven to have excellent performance as OER catalyst. The simultaneous introduction of Ni and Fe could adjust the electronic structures of the derived metal phosphides, producing low ohm resistance (R_0), low charge-transfer resistance (R_{ct}), and low OER activation energy, thus promoting charge transfer and accelerating catalysis kinetics. After the first CV cycle, the formation of highly OER-active layer could protect the phosphide phases in bulk from further oxidation. Excellent OER activity and long-time stability were achieved with an overpotential of 329 mV at 10 mA cm^{-2} and Tafel slope of 48.2 mV dec^{-1}, benefiting from the electronic structure evolution in the tricomponent metal phosphides as evidenced by XPS and XANES/EXAFS analysis [95].

All the examples mentioned above were converted to metal phosphides via calcination and subsequent phosphorization procedure. By direct pyrolysis of a layered phosphonate-based MOF (H_3LCo), a kind of cobalt phosphate carbon hybrid (Co–P–C) was prepared. This composite had high content of $Co_2P_2O_7$ consisting of di-μ-oxo bridged edge-sharing CoO_6 and CoO_5 polyhedrons. The distorted metal coordination geometry with longer Co–O and Co–Co distances would lower the activation barrier of the formation of O–O bond, thus favored OER process with a small overpotential of around 260 mV for reaching a current density of 10 mA cm^{-2} [96].

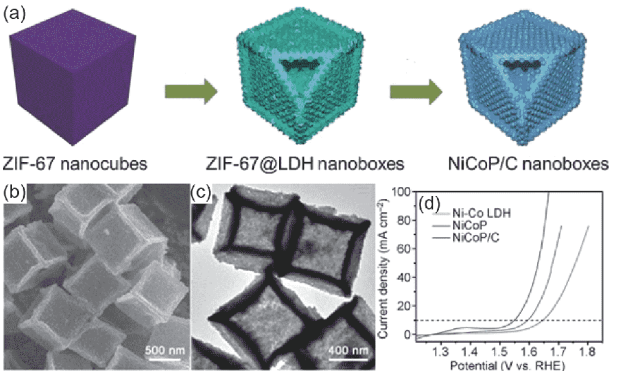

Figure 10 (a) Schematic illustration of the formation process of NiCoP/C nanoboxes. (b) FESEM image, (c) TEM image of NiCoP/C nanoboxes. (d) OER polarization curves of Ni–Co LDH, NiCoP, and NiCoP/C nanoboxes in an O_2-saturated 1.0 M KOH. Reprinted with permission from Ref. [94]. Copyright 2017 John Wiley and Sons (color online).

5 Conclusions

Since ORR and OER are two basic reactions in the electrochemical systems, developing catalysts with high activity, superior stability, and cost-efficiency is a forever pursuit. In virtue of the high surface area, diversity of the organic ligands, tunable metal nodes, and capacity to incorporate functional components, MOFs or their derived composites can serve as promising candidates for the ORR/OER process. Herein, we summarize recent research progress and strategies on MOF-based novel electrocatalysts for ORR and OER. Despite the extensive advances have been achieved (Tables 1, 2), most state-of-the-art catalysts still need large overpotentials of 0.25 to 0.4 V to reach the expected current density. Therefore, more researches are still needed and the following concerns are suggested for consideration in the future work.

(1) Development of active sites. Currently, precisely fabricated heteroatom-doped carbon, Fe/CoN_xC_y, Fe/Co@N_xC_y, and some transition metal single-atom active sites are mostly used in catalyzing ORR. For OER, Fe/Co/Ni-oxides, chalcogenides, and phosphides seem to be the major active components. The big MOFs family with rich chemical compositions and various tunability gives us great chances to expand the scope of active sites, not limited in the present stage. Further optimization and integration of the current systems should also be executed for better performance.

(2) Identification of active sites. Two strategies are generally accepted to improve the activity of catalyst: increasing

Table 1 Summary of ORR performance of MOF-based catalysts

Catalyst	Active sites	E_{onset} (V)	$E_{1/2}$ (V)	Ref.
NPC-1000	Doped-N	1.020	0.902	[47]
NGPC-1000-10	Doped-N	0.947	0.767	[37]
N,S-NH_3-C-7	Doped-N, S	–	0.837	[39]
MIL-88B-NH_3	Fe/FeC_3	1.030	0.920	[97]
Co@Co_3O_4@C-CM	Co/Co_3O_4	0.930	0.810	[98]
LDH@ZIF-67-800	Co–N	0.940	0.830	[99]
H-CoNC	Co–N_x	0.872	0.796	[53]
Co@NC-MOF-2-900	CoN_x–C_y and CoN_x	0.930	0.820	[63]
20Co-NC-1100	Co–N_4	0.930	0.800	[69]
C-Fe-Z_8-Ar	Fe–N_4	0.950	0.820	[65]
Fe-ZIF-50 nm	Fe–N_4	–	0.850	[68]

Table 2 Summary of OER performance of MOF-based catalysts

Catalyst	Active sites	η@10 mA cm^{-2} (mV)	Tafel slope (mV dec^{-1})	Ref.
FeNi@NCNT	FeNi alloy	300	48	[77]
2D Co_3O_4/CBDC	Co_3O_4	208	50	[81]
CoMo–H	CoO-MoO_2	312	69	[85]
NF@NC-$CoFe_2O_4$/C NRAs	$CoFe_2O_4$	240	45	[82]
Co_9S_8/NSCNFs-850	Co_9S_8	302	54	[86]
$CoSe_2$-450	$CoSe_2$	330	79	[88]
$CoTe_2$@NCNTFs	$CoTe_2$	330	83	[91]
CoP/rGO-400	CoP	340	66	[100]
NiCoP/C nanoboxes	NiCoP	330	96	[94]
H_3LCoCN800	$Co_2P_2O_7$	320	64	[96]

the number of active sites and increasing the intrinsic activity of the active sites. Therefore, identification of the nature of the active sites should be the first step to design the catalysts. *In-situ* characterization techniques and computational methods can give information about the reaction process and provide guidance for catalyst design.

(3) Structural design of catalysts. During the pyrolysis and post-modification process, the skeleton of MOFs may collapse and cause inevitable agglomeration, thus severely hinders the active sites. Recently, electrospinning and template-assist growth have been applied to the synthesis of MOFs. These approaches can notably increase the active sites and enhance the mass and electron transfer.

(4) Extension to industrial application. As yet, researches mainly focus on the performance of the catalysts at the laboratory application stage. A scalable process suitable for large scale production of low cost and high efficiency catalysts for actual industrial application is needed.

In summary, as emerging organic-inorganic hybrid porous materials, MOFs are promising precursors to fabricate electrocatalysts with unique characteristics for ORR and OER. Although there are still many challenges, the combination of experiment and theory will create new opportunities for discovery and breakthrough to the vast field of energy and environment-related applications.

Acknowledgements This work was supported by the National Natural Science Foundation of China (51825201), the National Key Research and Development Program of China (2017YFA0206701), the National Program for Support of Top-notch Young Professionals, and Changjiang Scholar Program.

Conflict of interest The authors declare that they have no conflict of interest.

1 Jiao Y, Zheng Y, Jaroniec M, Qiao SZ. *Chem Soc Rev*, 2015, 44: 2060–2086
2 Guan BY, Yu XY, Wu HB, Lou XWD. *Adv Mater*, 2017, 29: 1703614
3 Gupta S, Zhao S, Wang XX, Hwang S, Karakalos S, Devaguptapu SV, Mukherjee S, Su D, Xu H, Wu G. *ACS Catal*, 2017, 7: 8386–8393
4 Cheng Q, Han S, Mao K, Chen C, Yang L, Zou Z, Gu M, Hu Z, Yang H. *Nano Energy*, 2018, 52: 485–493
5 Stevens MB, Enman LJ, Batchellor AS, Cosby MR, Vise AE, Trang CDM, Boettcher SW. *Chem Mater*, 2016, 29: 120–140
6 Zhang L, Doyle-Davis K, Sun XL. *Energy Environ Sci*, 2019, https://doi.org/10.1039/c8ee02939c
7 Qian Y, Khan IA, Zhao D. *Small*, 2017, 13: 1701143
8 Furukawa H, Cordova KE, O'Keeffe M, Yaghi OM. *Science*, 2013, 341: 1230444
9 Zhang X, Chen A, Zhong M, Zhang ZH, Zhang X, Zhou Z, Bu XH. *Electrochem Energy Rev*, 2018, https://doi.org/10.1007/s41918-018-0024-x
10 Zhao Y, Song Z, Li X, Sun Q, Cheng N, Lawes S, Sun X. *Energy Storage Mater*, 2016, 2: 35–62
11 Gao M, Liu X, Yang H, Yu Y. *Sci China Chem*, 2018, 61: 1151–1158
12 Song Z, Cheng N, Lushington A, Sun X. *Catalysts*, 2016, 6: 116
13 Xia W, Mahmood A, Zou R, Xu Q. *Energy Environ Sci*, 2015, 8: 1837–1866
14 Zhang K, Qu C, Liang Z, Gao S, Zhang H, Zhu B, Meng W, Fu E, Zou R. *ACS Appl Mater Interfaces*, 2018, 10: 30460–30469
15 Yi FY, Zhang R, Wang H, Chen LF, Han L, Jiang HL, Xu Q. *Small Methods*, 2017, 1: 1700187
16 Huang ZF, Wang J, Peng Y, Jung CY, Fisher A, Wang X. *Adv Energy Mater*, 2017, 7: 1700544
17 Yeager E. *J Mol Catal*, 1986, 38: 5–25
18 Sanchez-Sanchez CM, Bard AJ. *Anal Chem*, 2009, 81: 8094–8100
19 Song CJ, Zhang JJ. *PEM Fuel Cell Electrocatalysts and Catalyst Layers*. Heidelberg: Springer, 2008. 89–134
20 Yu L, Pan X, Cao X, Hu P, Bao X. *J Catal*, 2011, 282: 183–190
21 Morozan A, Jousselme B, Palacin S. *Energy Environ Sci*, 2011, 4: 1238–1254
22 Shao M, Chang Q, Dodelet JP, Chenitz R. *Chem Rev*, 2016, 116: 3594–3657
23 Nørskov JK, Rossmeisl J, Logadottir A, Lindqvist L, Kitchin JR, Bligaard T, Jónsson H. *J Phys Chem B*, 2004, 108: 17886–17892
24 Man IC, Su HY, Calle-Vallejo F, Hansen HA, Martínez JI, Inoglu NG, Kitchin J, Jaramillo TF, Nørskov JK, Rossmeisl J. *ChemCatChem*, 2011, 3: 1159–1165
25 Dau H, Limberg C, Reier T, Risch M, Roggan S, Strasser P. *ChemCatChem*, 2010, 2: 724–761
26 Trasatti S. *Electrochim Acta*, 1984, 29: 1503–1512
27 Suntivich J, May KJ, Gasteiger HA, Goodenough JB, Shao-Horn Y. *Science*, 2011, 334: 1383–1385
28 Cho K, Han SH, Suh MP. *Angew Chem Int Ed*, 2016, 55: 15301–15305
29 Decoste JB, Peterson GW, Smith MW, Stone CA, Willis CR. *J Am Chem Soc*, 2012, 134: 1486–1489
30 Usov PM, Huffman B, Epley CC, Kessinger MC, Zhu J, Maza WA, Morris AJ. *ACS Appl Mater Interfaces*, 2017, 9: 33539–33543
31 Mao J, Yang L, Yu P, Wei X, Mao L. *Electrochem Commun*, 2012, 19: 29–31
32 Jiang M, Li L, Zhu D, Zhang H, Zhao X. *J Mater Chem A*, 2014, 2: 5323–5329
33 Sohrabi S, Dehghanpour S, Ghalkhani M. *ChemCatChem*, 2016, 8: 2356–2366
34 Jahan M, Bao Q, Loh KP. *J Am Chem Soc*, 2012, 134: 6707–6713
35 Wang H, Yin F, Chen B, Li G. *J Mater Chem A*, 2015, 3: 16168–16176
36 Banham D, Feng F, Pei K, Ye S, Birss V. *J Mater Chem A*, 2013, 1: 2812–2820
37 Zhang L, Su Z, Jiang F, Yang L, Qian J, Zhou Y, Li W, Hong M. *Nanoscale*, 2014, 6: 6590–6602
38 Zhong H, Wang J, Zhang Y, Xu W, Xing W, Xu D, Zhang Y, Zhang X. *Angew Chem Int Ed*, 2014, 53: 14235–14239
39 Song Z, Liu W, Cheng N, Norouzi Banis M, Li X, Sun Q, Xiao B, Liu Y, Lushington A, Li R, Liu L, Sun X. *Mater Horiz*, 2017, 4: 900–907
40 Wu M, Li C, Zhao J, Ling Y, Liu R. *Dalton Trans*, 2018, 47: 7812–7818
41 Wang Y, Tao L, Xiao Z, Chen R, Jiang Z, Wang S. *Adv Funct Mater*, 2018, 28: 1705356
42 Qian Y, An T, Birgersson KE, Liu Z, Zhao D. *Small*, 2018, 14: 1704169
43 Xuan C, Hou B, Xia W, Peng Z, Shen T, Xin HL, Zhang G, Wang D. *J Mater Chem A*, 2018, 6: 10731–10739
44 Wu M, Wang K, Yi M, Tong Y, Wang Y, Song S. *ACS Catal*, 2017, 7: 6082–6088
45 Shi PC, Yi JD, Liu TT, Li L, Zhang LJ, Sun CF, Wang YB, Huang YB, Cao R. *J Mater Chem A*, 2017, 5: 12322–12329
46 Chung DY, Lee KJ, Yu SH, Kim M, Lee SY, Kim OH, Park HJ, Sung YE. *Adv Energy Mater*, 2015, 5: 1401309
47 Ye L, Chai G, Wen Z. *Adv Funct Mater*, 2017, 27: 1606190
48 Kim IT, Shin S, Shin MW. *Carbon*, 2018, 135: 35–43

49 Zhang P, Sun F, Xiang Z, Shen Z, Yun J, Cao D. *Energy Environ Sci*, 2014, 7: 442–450
50 Pandiaraj S, Aiyappa HB, Banerjee R, Kurungot S. *Chem Commun*, 2014, 50: 3363–3366
51 Xia W, Zhu J, Guo W, An L, Xia D, Zou R. *J Mater Chem A*, 2014, 2: 11606–11613
52 You B, Jiang N, Sheng M, Drisdell WS, Yano J, Sun Y. *ACS Catal*, 2015, 5: 7068–7076
53 Song X, Guo L, Liao X, Liu J, Sun J, Li X. *Small*, 2017, 13: 1700238
54 Ahn SH, Klein MJ, Manthiram A. *Adv Energy Mater*, 2017, 7: 1601979
55 Wan X, Wu R, Deng J, Nie Y, Chen S, Ding W, Huang X, Wei Z. *J Mater Chem A*, 2018, 6: 3386–3390
56 Li Z, Shao M, Zhou L, Yang Q, Zhang C, Wei M, Evans DG, Duan X. *Nano Energy*, 2016, 25: 100–109
57 Wang R, Yan T, Han L, Chen G, Li H, Zhang J, Shi L, Zhang D. *J Mater Chem A*, 2018, 6: 5752–5761
58 Niu Q, Guo J, Chen B, Nie J, Guo X, Ma G. *Carbon*, 2017, 114: 250–260
59 Zhang J, Wu C, Huang M, Zhao Y, Li J, Guan L. *ChemCatChem*, 2018, 10: 1336–1343
60 Jasinski R. *Nature*, 1964, 201: 1212–1213
61 You S, Gong X, Wang W, Qi D, Wang X, Chen X, Ren N. *Adv Energy Mater*, 2016, 6: 1501497
62 Peera SG, Balamurugan J, Kim NH, Lee JH. *Small*, 2018, 14: 1800441
63 Collman JP, Devaraj NK, Decréau RA, Yang Y, Yan YL, Ebina W, Eberspacher TA, Chidsey CED. *Science*, 2007, 315: 1565–1568
64 Xiao M, Zhang H, Chen Y, Zhu J, Gao L, Jin Z, Ge J, Jiang Z, Chen S, Liu C, Xing W. *Nano Energy*, 2018, 46: 396–403
65 Wang X, Zhang H, Lin H, Gupta S, Wang C, Tao Z, Fu H, Wang T, Zheng J, Wu G, Li X. *Nano Energy*, 2016, 25: 110–119
66 Lai Q, Zheng L, Liang Y, He J, Zhao J, Chen J. *ACS Catal*, 2017, 7: 1655–1663
67 Li G, Zhang J, Li W, Fan K, Xu C. *Nanoscale*, 2018, 10: 9252–9260
68 Zhang H, Hwang S, Wang M, Feng Z, Karakalos S, Luo L, Qiao Z, Xie X, Wang C, Su D, Shao Y, Wu G. *J Am Chem Soc*, 2017, 139: 14143–14149
69 Wang XX, Cullen DA, Pan YT, Hwang S, Wang M, Feng Z, Wang J, Engelhard MH, Zhang H, He Y, Shao Y, Su D, More KL, Spendelow JS, Wu G. *Adv Mater*, 2018, 30: 1706758
70 Li JZ, Chen MJ, Cullen DA, Hwang S, Wang MY, Li BY, Liu KX, Karakalos S, Lucero M, Zhang HG, Lei C, Xu H, Sterbinsky GE, Feng ZX, Su D, More KL, Wang GF, Wang ZB, Wu G. *Nat Catal*, 2018, https://doi.org/10.1038/s41929-018-0164-8
71 Duan J, Chen S, Zhao C. *Nat Commun*, 2017, 8: 15341
72 Hai G, Jia X, Zhang K, Liu X, Wu Z, Wang G. *Nano Energy*, 2018, 44: 345–352
73 Zhao SL, Wang Y, Dong JC, He CT, Yin HJ, An PF, Zhao K, Zhang XF, Gao C, Zhang LJ, Lv JW, Wang JX, Zhang JQ, Khattak AM, Khan NA, Wei ZX, Zhang J, Liu SQ, Zhao HJ, Tang ZY. *Nat Energy*, 2016, 1: 16184
74 Li FL, Shao Q, Huang X, Lang JP. *Angew Chem Int Ed*, 2018, 57: 1888–1892
75 Xu Y, Tu W, Zhang B, Yin S, Huang Y, Kraft M, Xu R. *Adv Mater*, 2017, 29: 1605957
76 Sun H, Lian Y, Yang C, Xiong L, Qi P, Mu Q, Zhao X, Guo J, Deng Z, Peng Y. *Energy Environ Sci*, 2018, 11: 2363–2371
77 Tao Z, Wang T, Wang X, Zheng J, Li X. *ACS Appl Mater Interfaces*, 2016, 8: 35390–35397
78 Li X, Niu Z, Jiang J, Ai L. *J Mater Chem A*, 2016, 4: 3204–3209
79 Zhao J, Quan X, Chen S, Liu Y, Yu H. *ACS Appl Mater Interfaces*, 2017, 9: 28685–28694
80 Yang F, Zhao P, Hua X, Luo W, Cheng G, Xing W, Chen S. *J Mater Chem A*, 2016, 4: 16057–16063
81 Zhou J, Dou Y, Zhou A, Shu L, Chen Y, Li JR. *ACS Energy Lett*, 2018, 3: 1655–1661
82 Lu XF, Gu LF, Wang JW, Wu JX, Liao PQ, Li GR. *Adv Mater*, 2017, 29: 1604437
83 Xu H, Shi ZX, Tong YX, Li GR. *Adv Mater*, 2018, 30: 1705442
84 Huang T, Chen Y, Lee JM. *Small*, 2017, 13: 1702753
85 Lyu F, Bai Y, Li Z, Xu W, Wang Q, Mao J, Wang L, Zhang X, Yin Y. *Adv Funct Mater*, 2017, 27: 1702324
86 Wu LL, Wang QS, Li J, Long Y, Liu Y, Song SY, Zhang HJ. *Small*, 2018, 14: 1704035
87 Zhang X, Liu S, Zang Y, Liu R, Liu G, Wang G, Zhang Y, Zhang H, Zhao H. *Nano Energy*, 2016, 30: 93–102
88 Liu X, Liu Y, Fan LZ. *J Mater Chem A*, 2017, 5: 15310–15314
89 Li S, Peng S, Huang L, Cui X, Al-Enizi AM, Zheng G. *ACS Appl Mater Interfaces*, 2016, 8: 20534–20539
90 Xu B, Yang H, Yuan L, Sun Y, Chen Z, Li C. *J Power Sources*, 2017, 366: 193–199
91 Wang X, Huang X, Gao W, Tang Y, Jiang P, Lan K, Yang R, Wang B, Li R. *J Mater Chem A*, 2018, 6: 3684–3691
92 Liu M, Lu X, Guo C, Wang Z, Li Y, Lin Y, Zhou Y, Wang S, Zhang J. *ACS Appl Mater Interfaces*, 2017, 9: 36146–36153
93 Yan L, Cao L, Dai P, Gu X, Liu D, Li L, Wang Y, Zhao X. *Adv Funct Mater*, 2017, 27: 1703455
94 He P, Yu XY, Lou XWD. *Angew Chem Int Ed*, 2017, 56: 3897–3900
95 Wang M, Dong CL, Huang YC, Li Y, Shen S. *Small*, 2018, 14: 1801756
96 Zhou T, Du Y, Wang D, Yin S, Tu W, Chen Z, Borgna A, Xu R. *ACS Catal*, 2017, 7: 6000–6007
97 Zhao S, Yin H, Du L, He L, Zhao K, Chang L, Yin G, Zhao H, Liu S, Tang Z. *ACS Nano*, 2014, 8: 12660–12668
98 Xia W, Zou R, An L, Xia D, Guo S. *Energy Environ Sci*, 2015, 8: 568–576
99 Li Z, Shao M, Zhou L, Zhang R, Zhang C, Wei M, Evans DG, Duan X. *Adv Mater*, 2016, 28: 2337–2344
100 Jiao L, Zhou YX, Jiang HL. *Chem Sci*, 2016, 7: 1690–1695